Tracking the spread of chaos in the swinging Atwood's machine

Nick Tufillaro
aqualytics.eco
P.O. Box 1028
Corvallis, OR 97333
nick@aqualytics.eco
orcid #: 0009-0006-2896-8832

May 8, 2026

Abstract

Chaos is investigated in the swinging Atwood's machine (SAM) as the mass ratio, μ, decreases away from the integrable motion at $\mu = 3$ down to mostly chaotic dynamics at $\mu = 2.7$. The spread of chaos is characterized by combining a stability index with a Poincaré surface of section (SOS). An effective computational solution requires detailed consideration of a few numeric overflow issues. Once these are resolved, the computational study shows that the spread of chaos, in this parameter regime, is associated with a hyperbolic periodic "loop" orbit. The problem illustrates how to incorporate some computational physics considerations into a junior-level classical mechanics course.

1 Introduction

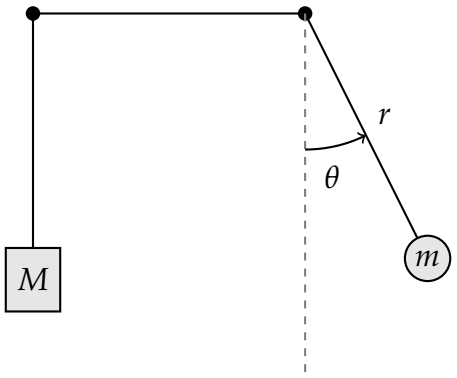

Figure 1: The swinging Atwood's machine.

The swinging Atwood's machine (SAM) is a tractable problem both theoretically [1] and experimentally [2, 3] for undergraduates studying classical mechanics. Recall that for SAM, one of the masses (m) is allowed to swing in the plane (Fig. 1). Assuming the masses are connected by frictionless, massless pulleys, the Hamiltonian for SAM is:

$$H = \frac{1}{2}\left(\frac{p_r^2}{\mu+1} + \frac{p_\theta^2}{r^2}\right) + gr(\mu - \cos\theta) \tag{1}$$

where p_r and p_θ are the conjugate momenta, g is gravitational acceleration, and $\mu = M/m$ is the mass ratio. We want to focus on how the dynamics depend on the parameter μ – so, without loss of generality, we set $m = 1$ in the Hamiltonian, which effectively just rescales the energy. Since the potential function is homogeneous, orbits at different energy levels are similar [4].

SAM is integrable for the mass ratio $\mu = 3$, and provably chaotic for all other mass ratios [5,6]. Integrable Hamiltonian systems are stratified by KAM tori [7], which allows for the solution of all periodic and quasiperiodic orbits in terms of the rotation number [8]. As we perturb away from this integrable motion, however, tori dissolve (based on stability conditions which are a function of the rotation number [9–11]), and stable regions of phase space (periodic or quasi-periodic orbits) are replaced by unstable regions (chaotic orbits).

In this paper, we examine how chaos spreads as the mass ratio decreases away from the integrable (stable) motion, specifically as mass decreases from 3 to 2.7. Numerical experiments reveal that the geometric feature governing the spread of chaos in this parameter regime is an unstable periodic orbit associated with a collision between the swinging mass and the pulley. In the lingo of dynamical systems, chaos spreads as part of the bifurcation process leading to the merger of an unstable homoclinic orbit and its elliptical partner – a saddle-center bifurcation of periodic orbits – and the regions of stable and chaotic orbits are roughly delineated by the stable and unstable manifolds of this homoclinic orbit [12]. From a physical point of view, this mechanism of chaos is easy to visualize – orbits that start very close are suddenly far apart after they fly off to the left, or to the right, during a near collision with the pulley. This is analogous to the origin of chaos in a forced pendulum, where orbits approaching the unstable equilibrium (the inverted pendulum) fall chaotically to the left or right, depending on the system's state.

To investigate chaos in SAM, we proceed in the normal way [13]. First, we visualize the global dynamics as a function of μ using a Poincaré surface of section (SOS) [14]. On the surface of section we identify stable regions (periodic or quasiperiodic orbits) and unstable regions (chaotic orbits), both qualitatively and quantitatively by coloring the orbit based on their stability, estimated using the Smaller Alignment Index (SALI) [15]. We identify geometrical structures in the phase space, namely the low-order periodic orbits and their stable and unstable manifolds, that shephard the flow as μ is varied from 3 (integrable) to 2.7 (mostly chaotic), and track the overall spread of chaos using the SALI. The theoretical and computational aspects are well covered in both pedagogical texts [16, 17] and commonly available numerical toolkits [18], so we will not delve much into the methods here, except for two aspects of the computational solution.

Namely, in Section 2, we discuss 'regularization' – or how to deal with the 'division by

zero' in the dynamical equations, and in Section 3, we discuss 'variational integration' – or how to handle overflow in the Jacobian Matrix through continuous normalization. After resolving these computational issues, we move on to Section 4, which presents the results on tracking the initial breakdown of the integrable motion. Although details vary from problem to problem, properly identifying and solving issues of overflow or underflow are ubiquitous in computational physics, and investigating the spread of chaos in SAM provides an introduction to some of the numeric challenges.

2 Fixing the collision singularity

To construct a SOS, we need to numerically solve trajectories for a long time. However, a severe numerical issue arises because as the swinging mass approaches the pulley ($r \to 0$), the angular velocity $\dot{\theta} = p_\theta / r^2$ rapidly approaches infinity. This $1/r^2$ singularity instantly crashes standard numerical ODE solvers due to infinite derivatives and truncation errors.

To fix this, we use the mathematical technique known as 'regularization' – originally developed for astronomical simulations [19] – which consists of introducing a new fictitious time variable, τ, which is related to physical time t by the transformation:

$$dt = r^2 d\tau \tag{2}$$

Using this, we construct an extended phase space Γ which includes physical time, t, as a state variable:

$$\Gamma = r^2(H - E) = \frac{r^2 p_r^2}{2(1+\mu)} + \frac{1}{2}p_\theta^2 + gr^3(\mu - \cos\theta) - Er^2 = 0 \tag{3}$$

With the new time τ, we obtain the regularized equations of motion (denoted by primes $d/d\tau$):

$$r' = \frac{\partial \Gamma}{\partial p_r} = \frac{r^2 p_r}{1+\mu} \tag{4}$$

$$\theta' = \frac{\partial \Gamma}{\partial p_\theta} = p_\theta \tag{5}$$

$$p_r' = -\frac{\partial \Gamma}{\partial r} = -\frac{r p_r^2}{1+\mu} - 3gr^2(\mu - \cos\theta) + 2Er \tag{6}$$

$$p_\theta' = -\frac{\partial \Gamma}{\partial \theta} = -gr^3 \sin\theta \tag{7}$$

$$t' = \frac{\partial \Gamma}{\partial(-E)} = r^2 \tag{8}$$

Even if the mass passes exactly through the pulley ($r = 0$), the right-hand sides remain well-behaved, transitioning without blowing up to infinity.

The new variable effectively slows down time near the collision. This makes fixed-step-size simulations very inefficient. Therefore, an adaptive step-size method is required to solve the equations using regularization. In this study, we used the Dormand-Prince

(RK45) method [20]. The adaptive solver shrinks or grows the step size in fictitious time τ by comparing the difference between the 4th and 5th-order to tight relative and absolute tolerances (10^{-8} and 10^{-10}, respectively).

A Poincaré surface of section reduces the complexity of the 4D phase space $(r, \theta, p_r, p_\theta)$ down to a 2D plot. Because energy, E, is conserved, the accessible states are restricted to a 3D "energy shell" [21]. We take a 2D "slice" through this shell by recording the system state only when it crosses a specific geometric plane. In our analysis this is defined at $\theta = 0$ (the pendulum hanging straight down) while the mass crosses moving in the positive angular direction ($p_\theta > 0$). The resulting intersections are plotted in the remaining coordinates (r, p_r), which define a (nonglobal) Poincaré surface of section.

Solving for a grid of initial conditions (r_0, p_{r0}) while varying μ (with fixed E) allows us to explore how the global dynamics depend on μ. Regions with continuous curves on the SOS indicate stable, quasi-periodic invariant tori, while scattered "dust" indicates unstable regions with chaotic orbits.

3 Distinguishing stable from unstable orbits

To evaluate the stability of an orbit, we look at the evolution of small perturbations using the "variational equations" constructed with the Jacobian matrix. Consider an n-dimensional continuous dynamical system defined by the system of ordinary differential equations:

$$\frac{d\mathbf{x}}{dt} = \mathbf{f}(\mathbf{x}(t)) \tag{9}$$

where $\mathbf{x} \in \mathbb{R}^n$ represents the state vector. Let $\mathbf{x}(t)$ be the reference trajectory, and $\mathbf{x}(t) + \mathbf{w}(t)$ be a perturbed trajectory. Linearizing the dynamics via a Taylor expansion yields the variational equations:

$$\frac{d\mathbf{w}}{dt} = J(\mathbf{x}(t))\,\mathbf{w}(t) \tag{10}$$

where $J(\mathbf{x}) = \frac{\partial \mathbf{f}}{\partial \mathbf{x}}$ is the $n \times n$ Jacobian matrix evaluated along the reference trajectory.

In a chaotic regime, the distance between infinitesimally close trajectories diverges exponentially. Mathematically, the magnitude of the deviation vector grows as $||\mathbf{w}(t)|| \sim e^{\lambda_1 t}$, where $\lambda_1 > 0$ is the Maximum Lyapunov Exponent. When integrating these equations numerically using standard double-precision floating-point arithmetic (which caps at approximately 10^{308}), chaotic orbits will cause $||\mathbf{w}(t)||$ to overflow, resulting in a `NaN` (Not a Number) system failure within seconds.

However, as described below, to distinguish chaotic orbits from stable orbits, we only need to track the *direction* of the deviation vectors, not their magnitude. So we can restrict the solver to integrating unit vectors $\hat{\mathbf{w}} = \mathbf{w}/||\mathbf{w}||$. While discrete normalization at each integration step is an option, a more mathematically elegant and numerically stable approach is continuous normalization built directly into the ODEs. Taking the time derivative of $\hat{\mathbf{w}}$:

$$\frac{d}{dt}\hat{\mathbf{w}} = \frac{d}{dt}\left(\frac{\mathbf{w}}{(\mathbf{w}^T\mathbf{w})^{1/2}}\right) \tag{11}$$

Applying the quotient rule and substituting $\dot{\mathbf{w}} = J\mathbf{w}$:

$$\frac{d\hat{\mathbf{w}}}{dt} = \frac{\dot{\mathbf{w}}}{||\mathbf{w}||} - \frac{\mathbf{w}}{||\mathbf{w}||^3}(\mathbf{w}^T\dot{\mathbf{w}}) = J\hat{\mathbf{w}} - \hat{\mathbf{w}}\left(\hat{\mathbf{w}}^T J\hat{\mathbf{w}}\right) \tag{12}$$

This equation acts as an intrinsic Gram-Schmidt orthogonal projection. The term $(\hat{\mathbf{w}}^T J\hat{\mathbf{w}})\hat{\mathbf{w}}$ subtracts any growth in the direction of $\hat{\mathbf{w}}$, mathematically guaranteeing that $\frac{d}{dt}||\hat{\mathbf{w}}||^2 = 0$. By appending this equation to the physical state equations, floating-point overflow is entirely eliminated.

The Smaller Alignment Index (SALI) method takes advantage of the stretching nature of chaotic phase space to quickly distinguish between stable and unstable orbits [15]. Suppose we initialize two independent, orthonormal deviation vectors, $\hat{\mathbf{w}}_1(0)$ and $\hat{\mathbf{w}}_2(0)$. In a stable/quasiperiodic orbit, the motion is confined to an invariant torus. Without an exponentially dominant stretching direction, the two deviation vectors fluctuate and drift, but they remain linearly independent and do not permanently align. In an unstable/chaotic orbit, the phase space possesses at least one direction of exponential stretching. As the system evolves, the flow aggressively pulls both $\hat{\mathbf{w}}_1$ and $\hat{\mathbf{w}}_2$ to point along the direction of maximal expansion. Because the vectors are normalized, they will either become identical (parallel) or exact opposites (anti-parallel) (Fig. 2).

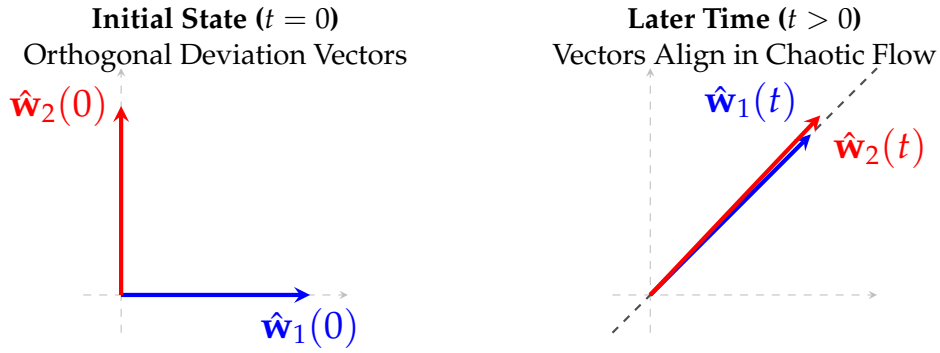

Figure 2: The Smaller Alignment Index (SALI) tracks alignment of perturbation vectors. Initially orthogonal vectors (left) are stretched by a chaotic flow (right), eventually aligning parallel to the axis of maximal expansion.

To quantify this geometric alignment, the Smaller Alignment Index is defined as the minimum between the sum and the difference of the two normalized deviation vectors:

$$\text{SALI}(t) = \min\left(||\hat{\mathbf{w}}_1(t) + \hat{\mathbf{w}}_2(t)||,\ ||\hat{\mathbf{w}}_1(t) - \hat{\mathbf{w}}_2(t)||\right) \tag{13}$$

If the vectors align parallel ($\hat{\mathbf{w}}_1 \to \hat{\mathbf{w}}_2$), their difference approaches zero. If they align anti-parallel ($\hat{\mathbf{w}}_1 \to -\hat{\mathbf{w}}_2$), their sum approaches zero. In either case, the SALI plummets.

4 Tracking the spread of chaos

To track the spread of chaos in SAM, we estimate the percentage of unstable orbits to the total number of orbits by numerically sampling phase space using the surface of section.

How this is accomplished is illustrated in Figure 3, which shows how the phase space contains a greater percentage of chaotic orbits as we move away from the integrable motion at $\mu = 3$ to $\mu = 2.9$, 2.8, and 2.7. The stability of each orbit in the SOS is evaluated

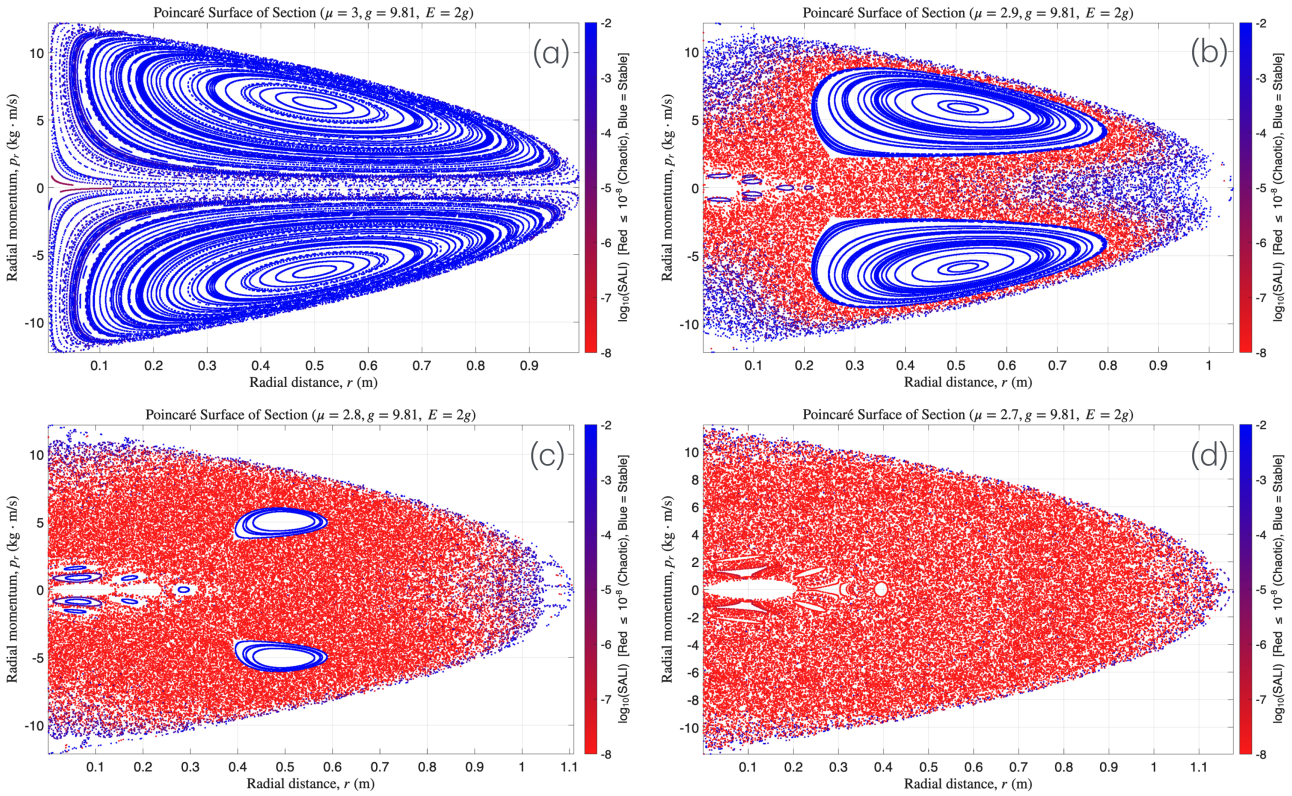

Figure 3: A sequence of surfaces of section for decreasing mass ratios (a) $\mu = 3$, integrable, stratified by tori (b) $\mu = 2.9$, nonintegrable, KAM tori and chaos (c) $\mu = 2.8$ (d) $\mu = 2.7$, mostly chaotic

and colored according to its estimated stablity index. In the color map, a blue hue indicates stability and a red hue instability. A single threshold is applied to the stability index ($\log_{10}(\text{SALI}) < -8$) to quantitatively evaluate the "spread" of chaos. The percentage is considered to be a simple estimate; a range of percentages is possible depending on the exact parameters chosen, however, the over all trends (increasing, decreasing) are assumed to be similar for reasonable choices of parameters.

Figure 4 shows a plot of the spread of chaos as μ decreases from 3 down to 2.7. As indicated by the visual inspection, the percentage of phase space occupied by chaotic orbits decreases (more or less) monotonically from $\mu = 3$ to 2.7. Indeed, with a basic grounding in dynamical systems, it is easy to identify the geometrical mechanism causing the spread of the chaos – namely a low-order hyperbolic periodic orbit that moves toward its partner elliptic periodic orbit, and in the process appears to destroy KAM tori as it approaches a saddle-center bifurcation, which the numerics indicate occurs at $\mu \approx 2.77$. This is an instance of what has been called "separatix chaos" [22, 23].

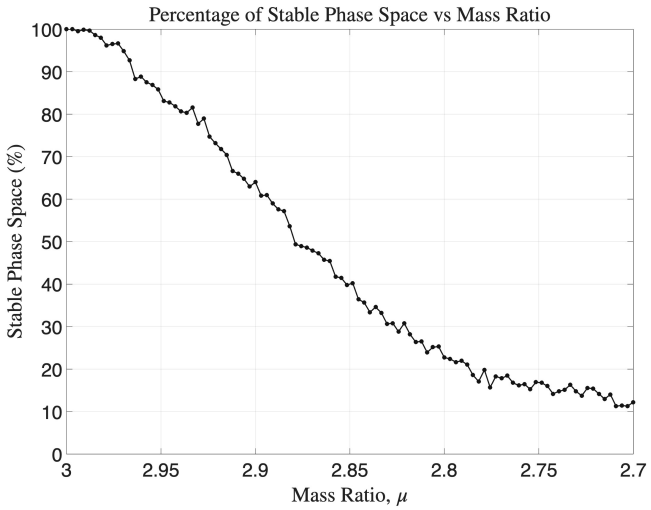

Figure 4: Estimated percentage of phase space with stable orbits as a function of the mass ratio, μ

In the study of dynamical systems, a "separatrix" is a boundary in phase space that divides distinct types of motion [24, 25]. Consider a pendulum [26, 27]. It has two primary modes of behavior: libration – small oscillations around the stable equilibrium (the bottom), and rotation – full circular revolutions (when given enough energy). The curve that separates these two behaviors is the separatrix. Physically, it represents the trajectory where the pendulum has exactly enough energy to reach the upright vertical position and stay there (an unstable equilibrium). In an ideal, integrable system (like the frictionless pendulum), the separatrix is a smooth, well-defined boundary. However, when a small perturbation is applied, the separatrix also points to a generic mechanism to generate chaos. The approach to the unstable position along the separatix (an unstable equilibrium point in the pendulum, or an unstable periodic orbit in SAM) can result in the system becoming extremely sensitive to even the smallest external influence near this boundary. The geometrical remnants of the separatrix in the perturbed system are the stable (W^s) and unstable manifolds (W^u). Regions near a hyperbolic point of phase space generate chaotic behavior because the flow is ripped apart near these geometric structures, and the way the flow comes back together can be extremely complicated as originally discovered by Poincaré [28]. According to the Smale-Birkhoff Homoclinic Theorem [29], if stable and unstable manifolds in the perturbed system intersect once transversally, they must intersect an infinite number of times, creating a "homoclinic tangle." This produces a region of "stochasticity" where the trajectory is chaotic, exhibiting sensitive dependence on initial conditions.

The hyperbolic point organizing the chaotic regions of SAM near the integrable mass ratio ($\mu = 3$) is easy to spot in the SOS. As shown in Figure 5 for $\mu = 2.95$, both the elliptic fixed point, and the hyperbolic fixed point, correspond to two separate, and coexisting, periodic "loop" orbits in configuration space. We call the stable orbit (blue curve in Fig. 5(b)) the "stable loop," and the hyperbolic orbit (red curve in Fig. 5(b) the "unstable loop."

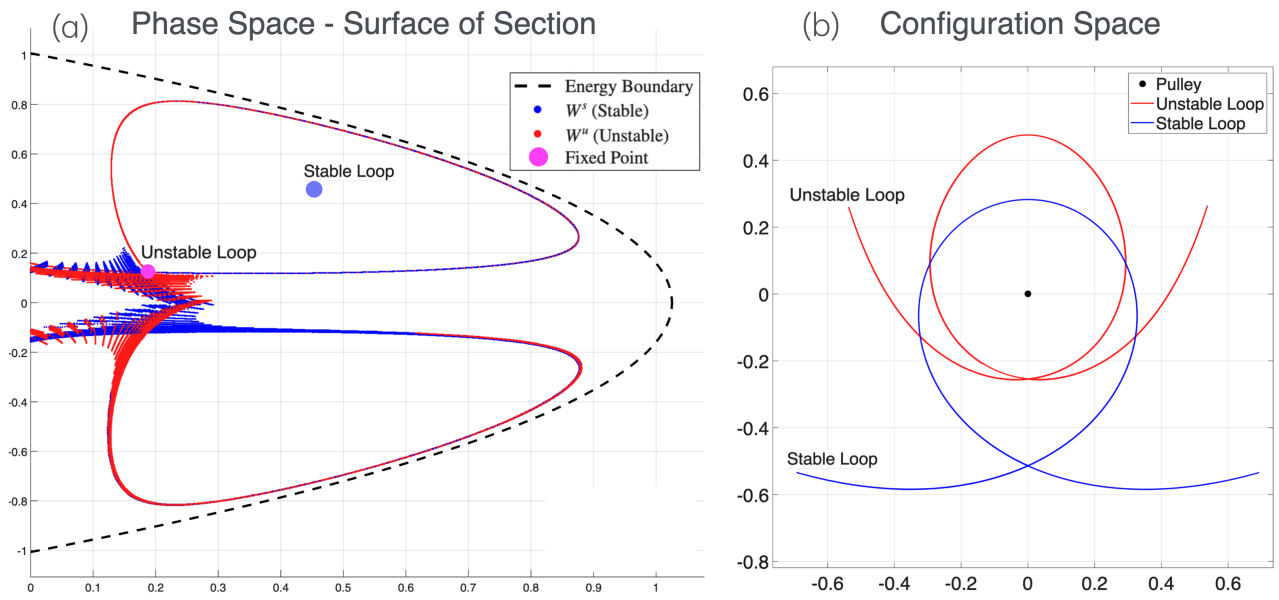

Figure 5: (a) The fixed points in phase space surface of section, and (b) their corresponding "loop" periodic orbits in configuration space. The stable loop orbit corresponds to an elliptic fixed point in phase space that organizes the main collection of KAM tori when $2.7 < \mu < 3$. Branches of the stable (W^s) and unstable (W^u) manifolds of the hyperbolic homoclinic point (purple point in (a)) delineate the main stable, and unstable, regions in phase space.

By analytic continuation, we can follow these orbits back to their integrable ($\mu = 3$) locations. The stable loop at $\mu = 3$ is the central fixed point in Fig. 3(a) surrounded by elliptic tori, while the unstable loop corresponds to an orbit that starts to fall directly above the pulley ($\theta_0 = \pi$), wraps tightly around the pulley once, and then shoots upward. When is reaches the top, it falls once again and repeats. As described in [8], when $\mu = 3.0$ all the orbits of SAM in phase space are pinched between two periodic orbits – in the middle there is a (singular tori) stable loop periodic orbit which has more or less the same shape as that shown in Fig. 5b (blue curve). On the outside in phase space, surrounding all the tori, is an unstable orbit like that shown in Fig. 5b (red curve). As μ approaches 3, in configuration space the unstable loop becomes more tightly bound around the pulley and the ends of the orbit face straight up.

The unstable loop – which in the limit $\mu = 3$ collides with the pulley – is the origin of most of the unstable motion in SAM for $\mu \in [2.77, 3)$.

5 Supplementary Material

The supplementary material package contains computer codes and simulations that produce Figures 3-5 and can be a useful starting point for students looking to further explore

SAM's dynamics, or similar Hamiltonian systems. For instance, does the golden ratio appear in the last torus [30]?

References

[1] Nivaldo A. Lemos. *Analytical mechanics*. Cambridge University Press, 2018.

[2] Olivier Pujol, José-Philippe Pérez, Jean-Pierre Ramis, Carles Simó, Sergi Simon, and Jacques-Arthur Weil. Swinging Atwood machine: experimental and numerical results, and a theoretical study. *Physica D: Nonlinear Phenomena*, 239(12):1067–1081, 2010.

[3] Nicholas Tufillaro. Smiles and teardrops. Reed College Undergraduate Thesis: https://aquahue.net/aquahue/papers/sam_00.pdf, 1982.

[4] Regilene Oliveira and Claudia Valls. Polynomial integrability of hamiltonian systems with homogeneous potentials of degree-k. *Physics Letters A*, 380(46):3876–3880, 2016.

[5] J. Casasayas, A. Nunes, and N. Tufillaro. Swinging Atwood's machine: integrability and dynamics. *Journal de Physique*, 51(16):1693–1702, 1990.

[6] Regina Martınez and Carles Simó. Non-integrability of the degenerate cases of the swinging Atwood's machine using higher order variational equations. *Discrete Contin. Dyn. Syst*, 29(1):1–24, 2011.

[7] Rafael De la Llave et al. A tutorial on KAM theory. In *Proceedings of Symposia in Pure Mathematics*, volume 69, pages 175–296. Providence, RI; American Mathematical Society; 1998, 2001.

[8] Ana Nunes, Josefina Casasayas, and Nicholas Tufillaro. Periodic orbits of the integrable swinging Atwood's machine. *American Journal of Physics*, 63(2):121–126, 02 1995.

[9] M. A. M. De Aguiar, Coraci Pereira Malta, M. Baranger, and K. T. R. Davies. Bifurcations of periodic trajectories in non-integrable Hamiltonian systems with two degrees of freedom: Numerical and analytical results. *Annals of Physics*, 180(2):167–205, 1987.

[10] M. A. M. De Aguiar and Michel Baranger. Invariant tori for two-dimensional non-integrable Hamiltonians. *Annals of Physics*, 186(2):355–380, 1988.

[11] K. Efstathiou and N. Voglis. A method for accurate computation of the rotation and the twist numbers of invariant circles. *Physica D: Nonlinear Phenomena*, 158(1-4):151–163, 2001.

[12] Robert L. Devaney. Homoclinic orbits in Hamiltonian systems. *J. Differential Equations*, 21(2):431–438, 1976.

[13] Carles Simó. Measuring the total amount of chaos in some hamiltonian systems. *Discrete and Continuous Dynamical Systems A*, 34:5135–5164, 2014.

[14] H. R. Dullin and A. Wittek. Complete Poincaré sections and tangent sets. *Journal of Physics A: Mathematical and General*, 28(24):7157–7180, 1995.

[15] Ch. Skokos, Ch. Antonopoulos, T.C. Bountis, and M.N. Vrahatis. Detecting order and chaos in Hamiltonian systems by the sali method. *Journal of Physics A: Mathematical and General*, 37(24):6269–6284, 2004.

[16] Nicholas B. Tufillaro, Tyler Abbott, and Jeremiah Reilly. *An experimental approach to nonlinear dynamics and chaos*. Addison-Wesley Redwood City, CA, 1992.

[17] Steven H. Strogatz. *Nonlinear dynamics and chaos: with applications to physics, biology, chemistry, and engineering*. Chapman and Hall/CRC, 2024.

[18] Matheus Rolim Sales, Leonardo Costa de Souza, Daniel Borin, Michele Mugnaine, José Danilo Szezech, Ricardo Luiz Viana, Iberê Luiz Caldas, Edson Denis Leonel, and Chris G Antonopoulos. pynamicalsys: A python toolkit for the analysis of dynamical systems. *Chaos, Solitons & Fractals*, 201:117269, 2025.

[19] Javier Roa. *Regularization in Orbital Mechanics: Theory and Practice*, volume 42. Walter de Gruyter GmbH & Co KG, 2017.

[20] Ernst Hairer, Gerhard Wanner, and Syvert P Nørsett. *Solving ordinary differential equations I: Nonstiff problems*. Springer, 1993.

[21] A. Ouazzani-TH. and M. Ouazzani-Jamil. Bifurcations of Liouville tori of an integrable case of swinging Atwood's machine. *Il Nuovo Cimento B (1971-1996)*, 110(9):1111–1121, 1995.

[22] G.M. Zaslavskiĭ and N.N. Filonenko. Stochastic instability of trapped particles and conditions of applicability of the quasi-linear approximation. *Soviet Journal of Experimental and Theoretical Physics*, 27:851, 1968.

[23] Regina Martínez and Carles Simó. Return maps, dynamical consequences and applications. *Qualitative theory of dynamical systems*, 14(2):353–379, 2015.

[24] Todd Timberlake. A computational approach to teaching conservative chaos. *American journal of physics*, 72(8):1002–1007, 2004.

[25] HJ Korsch, EM Graefe, and Hans-Jörg Jodl. The kicked rotor: Computer-based studies of chaotic dynamics. *American Journal of Physics*, 76(4):498–503, 2008.

[26] Robert DeSerio. Chaotic pendulum: The complete attractor. *American Journal of Physics*, 71(3):250–257, 2003.

[27] Pierre Coullet, Jean-Marc Gilli, Marc Monticelli, and Nicolas Vandenberghe. A damped pendulum forced with a constant torque. *American journal of physics*, 73(12):1122–1128, 2005.

[28] Henri Poincaré. *The three-body problem and the equations of dynamics: Poincaré's foundational work on dynamical systems theory*. Springer, 2017.

[29] Clark Robinson. *Dynamical systems: stability, symbolic dynamics, and chaos*. CRC press, 1998.

[30] Erik M. Bollt and James D. Meiss. Controlling chaotic transport through recurrence. *Physica D: Nonlinear Phenomena*, 81(3):280–294, 1995. This paper is dedicated to the memory of Dr. Erik Bollt (1967-2025).